interactions of multiple planets (*31*). The β Pic disk also displays a prominent inner warp (*5*, *19*), with a 3° to 4° tilt relative to the outer disk. Such a strong warp is not seen in the AU Mic disk, although its detectability would depend on its radial extent and orientation to the line of sight.

Since its discovery, the singular nature of the large scattered light disk around β Pic has raised the question of whether the system represents a typical phase in early disk evolution (*4*, *32*) or an anomalous occurrence, e.g., caused by the recent gravitational perturbation of a passing star (*6*). The discovery and characterization of the coeval AU Mic disk demonstrate that a common phase in disk evolution involves optically thin, asymmetric, bright scattered-light disks with multiple indications of substructure. Given that AU Mic and β Pic are members of the same moving group (*10*, *11*), the high degree of similarity between these two disks suggests that synchronous evolution has occurred.

Dust with sufficient optical depth to produce detectable scattered light spans a large range in radius around β Pic and AU Mic, from as close as ≈15 AU out to hundreds of AU. This is in contrast to older (≳200 My) debris disk systems, where the dust is confined to ringlike structures detected in submillimeter thermal emission (*33*, *34*) but not in scattered light (*35*, *36*). Recent simulations of evolving planetesimal disks are in accord with this observed morphological transformation from young dusty disks to old dusty rings (*37*). However, the young (~8 My) A star HR 4796A has its scattered light confined to a single bright ring (*38*), as opposed to a large disk, so stellar age cannot be the only factor governing disk morphology.

The spatially localized enhancements and deficits found in the AU Mic disk resemble the expected signposts of recent and/or ongoing planet formation in young disks. Simulations of planet formation by agglomeration find that bright rings of dust arise from gravitational stirring of planetesimals by recently formed planets of ≳1000-km radius (*37*, *39*). Dark gaps occur where the dust has been dynamically removed by planets or represent regions shadowed by interior rings that are optically thick. In this interpretation, the multiple structures present in the AU Mic disk suggest that planets massive enough to induce appreciable gravitational stirring form contemporaneously over a range of radii.

Finally, the stellar masses of β Pic (2 $M_{\odot}$) and AU Mic (0.5 $M_{\odot}$) straddle those of solar-mass stars. Hence, scrutiny of these two well-resolved disks may provide a window into the early solar system. The young Kuiper belt was about a factor of 100 more massive than its current state (*40*); its fractional dust luminosity would have been around 10^{-3} to 10^{-5} (*15*, *41*), comparable to that of the β Pic and AU Mic disks. This Keck AO study reveals that multiple dynamical substructures are common to optically thin disks at ages of ≈12 My. These structures may also reflect the dynamics that were active in the young Kuiper belt.

References and Notes

1. D. E. Backman, F. Paresce, in *Protostars and Planets III*, E. H. Levy, J. I. Lunine, Eds. (University of Arizona Press, Tucson, AZ, 1993), p. 1253.
2. A.-M. Lagrange, D. E. Backman, in *Protostars and Planets IV*, V. Mannings, A. P. Boss, S. S. Russell, Eds. (University of Arizona Press, Tucson, AZ, 2000), p. 639.
3. B. A. Smith, R. J. Terrile, *Science* **226**, 1421 (1984).
4. P. Artymowicz, *Annu. Rev. Earth Planet. Sci.* **25**, 175 (1997).
5. D. Mouillet *et al.*, *Mon. Not. R. Astron. Soc.* **292**, 896 (1997).
6. P. Kalas *et al.*, *Astrophys. J.* **530**, L133 (2000).
7. A. J. Weinberger *et al.*, *Astrophys. J.* **584**, L33 (2003).
8. Z. Wahhaj *et al.*, *Astrophys. J.* **584**, L27 (2003).
9. A. Brandeker *et al.*, *Astron. Astrophys.* **413**, 681 (2004).
10. D. Barrado y Navascués, *et al.*, *Astrophys. J.* **520**, L123 (1999).
11. B. Zuckerman *et al.*, *Astrophys. J.* **562**, L87 (2001).
12. M. A. C. Perryman *et al.*, *Astron. Astrophys.* **323**, L49 (1997).
13. M. C. Liu *et al.*, *Astrophys. J.* **608**, 526 (2004).
14. P. Kalas *et al.*, *Science* **303**, 1990 (2004).
15. D. C. Jewitt, J. X. Luu, in *Protostars and Planets IV*, V. Mannings, A. P. Boss, S. S. Russell, Eds. (University of Arizona Press, Tucson, AZ, 2000), p. 1201.
16. P. Wizinowich *et al.*, *Pub. Astron. Soc. Pac.* **112**, 315 (2000).
17. S. E. Persson *et al.*, *Astron. J.* **116**, 2475 (1998).
18. Materials and methods are available as supporting material on *Science* Online.
19. S. R. Heap *et al.*, *Astrophys. J.* **539**, 435 (2000).
20. G. Schneider, M. D. Silverstone, *Proc. SPIE* **4860**, 1 (2003).
21. P. Kalas, D. Jewitt, *Astron. J.* **110**, 794 (1995).
22. P. Artymowicz, M. Clampin, *Astrophys. J.* **490**, 863 (1997).
23. J. Liou, H. A. Zook, *Astron. J.* **118**, 580 (1999).
24. L. M. Ozernoy *et al.*, *Astrophys. J.* **537**, L147 (2000).
25. D. A. Golimowski *et al.*, *Astrophys. J.* **411**, L41 (1993).
26. D. P. Whitmire *et al.*, *Astron. Astrophys.* **203**, L13 (1988).
27. J. C. Augereau, R. P. Nelson, A. M. Lagrange, J. C. B. Papaloizou, D. Mouillet, *Astron. Astrophys.* **370**, 447 (2001).
28. A. Lecavelier Des Etangs, A. Vidal-Madjar, R. Ferlet, *Astron. Astrophys.* **307**, 542 (1996).
29. J. J. Lissauer, *Icarus* **69**, 249 (1987).
30. I. Sheret, W. R. F. Dent, M. C. Wyatt, *Mon. Not. R. Astron. Soc.* **348**, 1282 (2004).
31. E. W. Thommes, J. J. Lissauer, *Astrophys. J.* **597**, 566 (2003).
32. M. Jura *et al.*, *Astrophys. J.* **505**, 897 (1998).
33. J. S. Greaves *et al.*, *Astrophys. J.* **506**, L133 (1998).
34. W. S. Holland *et al.*, *Nature* **392**, 788 (1998).
35. B. A. Smith, J. W. Fountain, R. J. Terrile, *Astron. Astrophys.* **261**, 499 (1992).
36. P. Kalas, D. Jewitt, *Astron. J.* **111**, 1347 (1996).
37. S. J. Kenyon, B. C. Bromley, *Astron. J.* **127**, 513 (2004).
38. G. Schneider *et al.*, *Astrophys. J.* **513**, L127 (1999).
39. S. J. Kenyon, B. C. Bromley, *Astrophys. J.* **577**, L35 (2002).
40. S. A. Stern, J. E. Colwell, *Astron. J.* **114**, 841 (1997).
41. C. Dominik, G. Decin, *Astrophys. J.* **598**, 626 (2003).

42. I thank E. Chiang, G. Herczeg, M. Jura, P. Kalas, J. Krist, J. Linsky, and B. Macintosh for enlightening discussions. I am very grateful to A. Bouchez, D. LeMignant, R. Campbell, P. Wizinowich, and the staff of Keck Observatory for their assistance with the observations. This research has made use of the NASA/IPAC, 2MASS, and SIMBAD databases. I acknowledge support from NSF grant AST04-07441 and NASA grant HST-GO-09845.01-A.

Supporting Online Material
www.sciencemag.org/cgi/content/full/1102929/DC1
Materials and Methods

19 July 2004; accepted 4 August 2004
Published online 12 August 2004;
10.1126/science.1102929
Include this information when citing this paper.

Electrically Driven Single-Cell Photonic Crystal Laser

Hong-Gyu Park,[1] Se-Heon Kim,[1] Soon-Hong Kwon,[1] Young-Gu Ju,[2] Jin-Kyu Yang,[1] Jong-Hwa Baek,[1] Sung-Bock Kim,[2] Yong-Hee Lee[1]*

We report the experimental demonstration of an electrically driven, single-mode, low threshold current (~260 μA) photonic band gap laser operating at room temperature. The electrical current pulse is injected through a sub-micrometer-sized semiconductor wire at the center of the mode with minimal degradation of the quality factor. The actual mode of interest operates in a nondegenerate monopole mode, as evidenced through the comparison of the measurement with the computation based on the actual fabricated structural parameters. As a small step toward a thresholdless laser or a single photon source, this wavelength-size photonic crystal laser may be of interest to photonic crystals, cavity quantum electrodynamics, and quantum information communities.

The laser physics and quantum optics communities have been interested for some time in extremely small, low-loss, low-power lasers (*1*–*3*). The potential to localize photons into photonic band gap semiconductor microcavities having wavelength-scale volumes and high quality factors enables us to study the cavity quantum electrodynamics in solids and to construct quantum optical devices such as on-demand single photon sources. Several optically pumped, ultra-small, photonic crystal lasers (*4*–*8*) or electrically driven light-emitting structures using the concept of photonic crystals (*9*–*11*) have been recently reported. Two kinds of electrically driven photonic band edge lasers, large-volume lasers with high output power

[1]Department of Physics, Korea Advanced Institute of Science and Technology, Daejeon 305-701, Korea. [2]Telecommunication Basic Research Laboratory, Electronics and Telecommunications Research Institute, Daejeon 305-600, Korea.

*To whom correspondence should be addressed. E-mail: yhlee@kaist.ac.kr

(*12*) and quantum cascade lasers (*13*), especially draw our attention. However, the electronic activation of the wavelength-scale single-cell laser operating in a single mode, a crucial step toward a practical form of the thresholdless laser, has yet to be demonstrated.

One of the most daunting problems in trying to implement a single-cell, free-standing slab photonic crystal laser (*4*–*7*) is how to make electrical contact with the sub-micrometer-sized photonic crystal resonator structure (*14*). Locating the proper region inside the laser cavity to position an electrical contact requires an understanding of the resonant modes that are available in a single-cell triangular lattice photonic crystal cavity (*15*). Three potential candidates, each with a central node, were considered, because the introduction of a small central post as an electrical contact did not notably degrade the quality (*Q*) factor of the mode (*15*). The small central post functions as an electrical wire, a mode selector, and a heat sinker at the same time (*16*).

A sub-micrometer-sized semiconductor post is placed at the center of the single-cell photonic crystal resonator (Fig. 1A). The thickness of the semiconductor slab is 282.5 nm. Electrons are supplied laterally from the top electrode, whereas holes are injected directly through the bottom post. The carriers recombine in the six strain-compensated InGaAsP quantum wells that are designed to have an electroluminescence (EL) peak near communications wavelength of 1.5 μm. A doping structure that is inverted from that of a typical semiconductor laser is used to exploit the low mobility of the holes that are funneled through the sub-micrometer-sized post. The introduction of this heterojunction *n-i-p* structure also limits the occurrence of bimolecular recombination to the proximity of the central post and promotes an efficient overlap of the optical gain region with the mode profile. In addition, the modified single-cell photonic crystal cavity is surrounded by five heterogeneous photonic crystal lattices with the same lattice constant (*a*) but different air-hole sizes to improve the position and size of the central InP post (Fig. 2A). The peripheral dielectric material underneath the slab was added for mechanical support.

The fabrication procedure contains two main steps: the mesa formation and the definition of photonic crystal patterns (*17*). The scanning electron microscope (SEM), cross-sectional view in Fig. 1B shows a fabricated sub-micrometer-sized InP post. It was discovered that the speed of wet etching depends on the radii of the air holes and that the position and size of the post can be improved by systematically modifying the size distribution of the air holes. This chirped photonic crystal resonator structure improves the *Q* factor slightly; however, the resonant frequency and the modal volume of the relevant modes remain almost unchanged. This was confirmed by a three-dimensional (3D) finite-difference time-domain (FDTD) calculation.

The fabricated single-cell photonic crystal cavities are electrically pulse-pumped at room temperature. The width and the period of the injected electrical current pulse are ~6 ns and 2.5 μs, respectively (*18*). The emitted photons are collected by a 50× microscope objective lens with a numerical aperture of 0.42 and fed to a spectrometer. Single-mode lasing action was observed at a wavelength of 1519.7 nm (Fig. 3A). Above the threshold, a spectrometer-limited linewidth of 0.5 nm was measured from this nondegenerate lasing mode. The mode profile as captured by an infrared (IR) camera (Fig. 2B) exhibits a central intensity minimum and the characteristic features of a monopole mode (*5*, *15*). Monopole mode operation was confirmed by comparing the measured resonant frequencies with those obtained from the 3D FDTD calculation. Numerical structural input data directly from the SEM image were used in the FDTD computation to truthfully compensate for any fabrication imperfections. In addition, no preferred direction of polarization is observed from the top, as expected from the monopole mode (*5*).

The calculated field profiles associated with the monopole mode are shown in Fig. 2, C and D. The measured near-field profile (Fig. 2B) represents the intensity of the propagating field in the proximity of the slab within the depth of focus of the 50× objective and compares well with the vertical component of the Poynting vector computed at a plane 3.0 μm above the laser cavity that has a small post (Fig. 2C). Even the asymmetry originating from the imperfect fabrication is reasonably reproduced in the FDTD computation with the use of numerical structural input data. As a reference, the energy distribution confined in the slab is shown in Fig. 2D.

Among several theoretically identified resonant modes in the lattice parameters of Fig. 2A, only the monopole mode was experimentally observed with a gain spectrum and resonant frequency in agreement with theoretic predictions. This is attributed to the fact that the other potential central node modes, such as quadrupole or hexapole modes (*15*), are located outside the spectral gain region. No adjustable parameter was used in our computation.

The measured *Q* factor of a cold cavity for the monopole mode, as estimated from the spectral line width associated with a transparent current of ~225 μA (*8*), is ~>2500 and compares well with the computed *Q* factor of ~3480 obtained with a diamond-like post with 0.64*a* by 0.51*a* estimated from the SEM picture, where *a* is the lattice constant. The *Q* factor degrades rapidly when the post size becomes larger

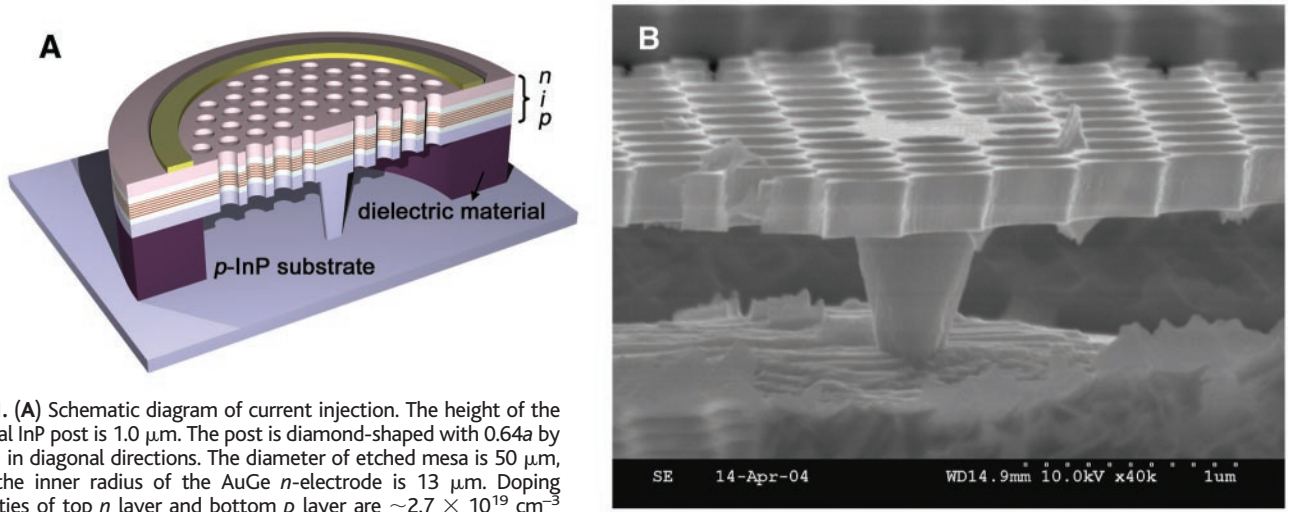

Fig. 1. (**A**) Schematic diagram of current injection. The height of the central InP post is 1.0 μm. The post is diamond-shaped with 0.64*a* by 0.51*a* in diagonal directions. The diameter of etched mesa is 50 μm, and the inner radius of the AuGe *n*-electrode is 13 μm. Doping densities of top *n* layer and bottom *p* layer are ~2.7×10^{19} cm^{-3} and ~2.5×10^{18} cm^{-3}, respectively. (**B**) Cross-sectional SEM image. From an intentionally broken sample, the region around the central post is clearly shown. Dusts around the post are remnants of the dielectric material, a photoresist, which are produced in the breaking process.

than the above value and improves slightly with smaller post size; however, the smaller post size leads to electrical resistance and thermal problems. Thus, it is important to optimize the post size considering both the optical and electrical characteristics.

The modal volume, V, of the monopole mode is found to be 5.87×10^{-2} μm^3. This value corresponds to 0.684 $(\lambda/n)^3$, where n is the refractive index of the slab material (3.4) and approaches the smallest theoretical value (*4*). The large estimated Purcell factor (389) of the current resonator implies the possibility of observing cavity quantum electrodynamic effects in an electrically driven, small, high Q cavity, photonic crystal laser (*1*).

A low threshold current of ~260 μA was observed from the peak output intensity (Fig. 3A) and compares favorably with those estimated in the optical pumping experiment (*5*–*8*). Considering that there are nonnegligible current leakage paths in the structure, the actual threshold current may be even smaller.

The soft turn-on shoulder near the threshold (Fig. 3A) implies a large spontaneous emission factor (β). The β value can be estimated from simple laser rate equations, given the experimental values and typical parameters of InGaAsP quantum wells (*15*, *19*). The critical parameter, such as the active surface area, is measured directly from the shape and size of the electroluminescent image obtained near the transparency. We found the β value is determined mostly by the shape of the light-current (L-*I*) curve below and near threshold, where slight variations of the parameters other than the surface recombination are tolerable. A β value of ~0.25 can be calculated by comparing measured spectrally integrated output intensities with L-*I* curves obtained from the rate equation (Fig. 3B). This β value is considerably higher than previously reported from the semiconductor nanolasers (*15*, *19*, *20*) and attributed to the effective carrier localization by electrical pumping together with the nondegeneracy and the small modal volume (*21*, *22*).

Typical electrical characteristics for a single-cell photonic crystal laser are shown (Fig. 3B, inset), where peak voltage and current values are used. The turn-on voltage is less than 1.0 V, and the electrical resistance is ~2.2 kΩ. Noticeable current leakage is identified from the (I dV/dI) curve. The relatively high resistance is mainly attributed to the sub-micrometer size of the p-InP post and partly attributed to the lateral distance between the n electrode and the center. The current leakage is attributed to the nonradiative recombination at the air-semiconductor air hole interfaces and at the edge of the mesa (*23*).

There are various issues still remain to be addressed before this electrically driven, ultrasmall cavity with a large Purcell factor becomes the practical on-demand single photon source. For example, one needs to find ways to place well-defined quantum dots or impurity atoms (*24*) at the antinode of the cavity and to inject

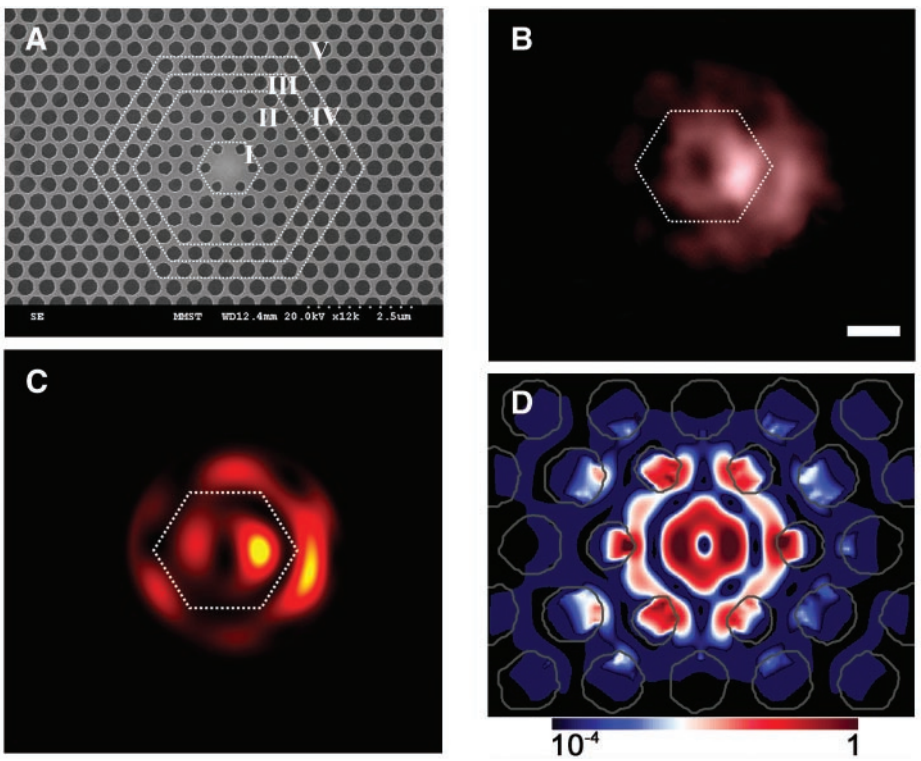

Fig. 2. (**A**) Top view of fabricated sample. The lattice constant, a, is ~510 nm, and the radii of the air holes in regions I, II, III, IV, and V are 0.28a, 0.35a, 0.385a, 0.4a, and 0.41a, respectively. (**B**) Monopole-mode image captured by an IR camera. The white bar represents 2-μm ruler. The white hexagon corresponds to region II-III interface in (A). (**C**) The vertical component of the Poynting vector obtained with the use of the structural data of (A) by 3D FDTD calculation. The calculation is performed at a vertical position of 3.0 μm above the slab, with consideration of a blurring effect by the objective lens. (**D**) The electric field intensity profile of the monopole mode calculated at the center of the slab (log scale).

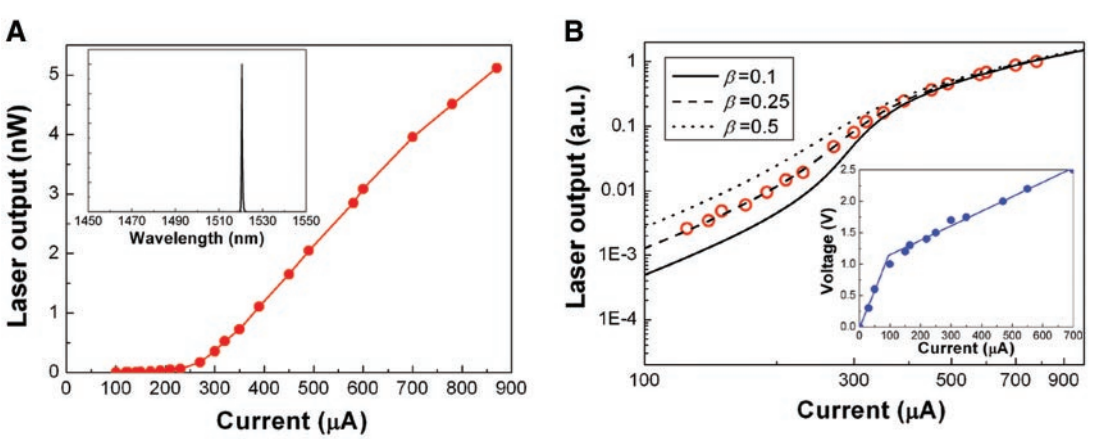

Fig. 3. (**A**) Typical L-I curve of the monopole-mode laser. Threshold current is ~260 μA, and output power indicates the peak value measured at the spectrometer. (Inset) The spectrum is taken at 700 μA. (**B**) Comparison of the measured L-I curves (red dots) with those obtained from the rate equations (black lines) for the monopole mode. Main parameters are as follows: internal efficiency η_i = 0.25, confinement factor Γ = 0.175, surface recombination velocity $v_s = 1.2 \times 10^4$ cm s^{-1}, bimolecular radiative coefficient $B = 1.6 \times 10^{-10}$ cm^3 s^{-1}, Auger coefficient $C = 5.0 \times 10^{-29}$ cm^6 s^{-1}, transparent carrier density $N_{tr} = 1.5 \times 10^{18}$ cm^{-3}, active volume $V_a = 1.72 \times 10^{-13}$ cm^3 and active surface area $A_a = 1.47 \times 10^{-8}$ cm^2. (Inset) Typical electrical characteristics are shown. a.u., arbitrary units.

single electron-hole pairs efficiently (*25*). The vertical coupling efficiency out of the cavity should be also improved by proper modifications of the cavity structure, e.g., the size of the air holes (*26*) and/or the reflectivity of the substrate. Alternatively, the photons localized in the cavity could be funneled horizontally into the neighboring low-loss photonic crystal waveguide (*27*) prepared by the quantum well intermixing (*28*). Together with all the challenging issues, the demonstration of electrically driven single-cell photonic crystal laser is believed to represent a small but meaningful step toward the ultimate photon source.

References and Notes

1. K. J. Vahala, *Nature* **424**, 839 (2003).
2. E. Yablonovitch, *Phys. Rev. Lett.* **58**, 2059 (1987).
3. T. F. Krauss, R. M. De La Rue, *Prog. Quantum Electron.* **23**, 51 (1999).
4. O. Painter *et al.*, *Science* **284**, 1819 (1999).
5. H. G. Park *et al.*, *Appl. Phys. Lett.* **79**, 3032 (2001).
6. H. Y. Ryu *et al.*, *Appl. Phys. Lett.* **80**, 3883 (2002).
7. M. Loncar, T. Yoshie, A. Scherer, P. Gogna, Y. Qiu, *Appl. Phys. Lett.* **81**, 2680 (2002).
8. K. Srinivasan *et al.*, *Appl. Phys. Lett.* **83**, 1915 (2003).
9. W. D. Zhou *et al.*, *IEEE J. Quantum Electron.* **37**, 1153 (2001).
10. D. S. Song, S. H. Kim, H. G. Park, C. K. Kim, Y. H. Lee, *Appl. Phys. Lett.* **80**, 3901 (2002).
11. T. D. Happ *et al.*, *Appl. Phys. Lett.* **82**, 4 (2003).
12. S. Noda, M. Yokoyama, M. Imada, A. Chutinan, M. Mochizuki, *Science* **293**, 1123 (2001).
13. R. Colombelli *et al.*, *Science* **302**, 1374 (2003); published online 30 October 2003; 10.1126/science.1090561.
14. A. F. J. Levi *et al.*, *Electron. Lett.* **28**, 1010 (1992).
15. H. G. Park *et al.*, *IEEE J. Quantum Electron.* **38**, 1353 (2002).
16. H. G. Park *et al.*, *IEEE Photonics Technol. Lett.* **15**, 1327 (2003).
17. Materials and methods are available as supporting material on *Science* Online.
18. The large thermal resistance (346 K mW^{-1}) of the post structure is responsible for this small duty cycle.
19. M. Fujita, R. Ushigome, T. Baba, *IEEE Photonics Technol. Lett.* **13**, 403 (2001).
20. R. E. Slusher *et al.*, *Appl. Phys. Lett.* **63**, 1310 (1993).
21. H. Yokoyama, *Science* **256**, 66 (1992).
22. J. Vuckovic *et al.*, *IEEE J. Quantum Electron.* **35**, 1168 (1999).
23. L. A. Coldren, S. W. Corzine, *Diode Lasers and Photonic Integrated Circuits* (Wiley, New York, 1995).
24. Z. Yuan *et al.*, *Science* **295**, 102 (2002); published online 13 December 2001; 10.1126/science.1066790.
25. J. Kim, O. Benson, H. Kan, Y. Yamamoto, *Nature* **397**, 500 (1999).
26. S. H. Kim, S. K. Kim, Y. H. Lee, unpublished data.
27. S. Noda, A. Chutinan, M. Imada, *Nature* **407**, 608 (2000).
28. D. G. Deppe, N. Holonyak Jr., *J. Appl. Phys.* **64**, R93 (1988)

29. This work was supported by the National Research Laboratory Project of Korea and the National Research and Development Project for Nano Science and Technology.

Supporting Online Material

www.sciencemag.org/cgi/content/full/305/5689/1444/DC1

Materials and Methods

Figs. S1 to S4

1 June 2004; accepted 29 July 2004

Macroscopic, Neat, Single-Walled Carbon Nanotube Fibers

Lars M. Ericson,[1,2] Hua Fan,[1,2] Haiqing Peng,[1,2] Virginia A. Davis,[1,3] Wei Zhou,[5] Joseph Sulpizio,[1,2] Yuhuang Wang,[1,2] Richard Booker,[1,2] Juraj Vavro,[5] Csaba Guthy,[5] A. Nicholas G. Parra-Vasquez,[1,3] Myung Jong Kim,[1,2] Sivarajan Ramesh,[1,2] Rajesh K. Saini,[1,4] Carter Kittrell,[1,2] Gerry Lavin,[6] Howard Schmidt,[1,2] W. Wade Adams,[1,2] W. E. Billups,[1,4] Matteo Pasquali,[1,3] Wen-Fang Hwang,[1,2]* Robert H. Hauge,[1,2] John E. Fischer,[5] Richard E. Smalley[1,2]*

Well-aligned macroscopic fibers composed solely of single-walled carbon nanotubes (SWNTs) were produced by conventional spinning. Fuming sulfuric acid charges SWNTs and promotes their ordering into an aligned phase of individual mobile SWNTs surrounded by acid anions. This ordered dispersion was extruded via solution spinning into continuous lengths of macroscopic neat SWNT fibers. Such fibers possess interesting structural composition and physical properties.

Individual single-walled carbon nanotubes (SWNTs) possess remarkable mechanical (*1–3*), electrical (*4–6*), and thermal (*7*, *8*) properties that equal, or even surpass, those of other benchmark materials (steel, copper, and diamond, respectively). Applications on the nanometer and micrometer scale, such as SWNT-based transistors (*9*) and chemical sensors (*10*), are progressing rapidly. To date, SWNT composite fibers have been produced that show notable mechanical reinforcement (*11–13*) or improvements in otherwise marginal transport properties (*14*). However, they still fall far short of the impressive properties of individual SWNTs. Neat SWNT fibers have only been produced in relatively short centimeter lengths through laboratory processes with limited industrial scalability (*15–17*), or have been produced in continuous lengths during the nanotube synthesis process, with high levels of impurities and marginal alignment (*18*). Starting with purified SWNTs, we have produced well-aligned continuous macroscopic fibers, without any supporting surfactant or polymer structure. Fibers were made from concentrated dispersions of SWNTs in 102% sulfuric acid via an industrially viable wet spinning technique.

Because of the high temperature stability of SWNTs, melt spinning is not an option. Wet spinning is the only viable approach, as is the case for conventional rodlike polymers such as poly(p-phenylene benzobisoxazole) (PBO), poly(p-phenylene terephthalamide) (PPTA), and poly(p-phenylene benzobisthiazole) (PBZT). The main challenge to the production of neat SWNT fibers is dispersing the SWNTs at high enough concentrations suitable for efficient alignment and effective coagulation. However, because of their chemical inertness and strong intertube van der Waals attractions, SWNTs aggregate into ropes with limited solubility in aqueous, organic, or acidic media. Even in stable organic (such as dimethyl formamide or dichlorobenzene) or surfactant-aided aqueous (such as sodium dodecyl sulfate or Triton X-100) dispersions, SWNTs are typically limited to low concentrations of nanotube bundles. If a surfactant is used to disperse the SWNTs, there is the added complication of removing the surfactant from the fiber during coagulation or after processing. In superacids (100+% sulfuric acid), SWNTs form charge-transfer complexes of individual positively charged nanotubes surrounded by a finite number of sulfuric acid anions (*19*). At very low concentration, such charged tube–anion complexes behave as Brownian rods (*20*). At higher concentration [>0.03 weight % (wt%)], a small amount of dissolved individual tubes coexists with a SWNT spaghetti phase consisting of seemingly endless "swollen" ropes of well-aligned positively charged SWNTs intercalated by sulfuric acid anions (*19*). The SWNTs in the spaghetti are mobile and at a high enough concentration (>4 wt%), they coalesce and form ordered domains (*20*), behaving similarly to nematic liquid crystalline rodlike polymers. The SWNT/acid system is very sensitive to water; the introduction of even minimal moisture causes phase separation and the precipitation of discrete needle-like crystal solvates,

[1]Center for Nanoscale Science and Technology, [2]Carbon Nanotechnology Laboratory, [3]Department of Chemical Engineering, [4]Department of Chemistry, Rice University, Houston, TX 77005, USA. [5]Department of Materials Science and Engineering, University of Pennsylvania, Philadelphia, PA 19104, USA. [6]Carbon Consultations, 15 Wellesley Road, Swarthmore, PA 19081, USA.

*To whom correspondence should be addressed. E-mail: whwang@rice.edu (W.F.H.); smalley@rice.edu (R.E.S.)